Simultaneous photoreduction of Uranium(VI) and photooxidation of Arsenic (III) in aqueous solution over g-C$_3$N$_4$/TiO$_2$ heterostructured catalysts under simulated sunlight irradiation

Xun-Heng Jiang[a], Qiu-Ju Xing[a], Xu-Biao Luo[a], Fei Li[a], Jian-Ping Zou[a,*], Shan-Shan Liu[a], Xiang Li[a], Xiang-Ke Wang[b,*]

[a] Key Laboratory of Jiangxi Province for Persistent Pollutants Control and Resources Recycle, Nanchang Hangkong University, Nanchang 330063, PR China
[b] School of Environment and Chemical Engineering, North China Electric Power University, Beijing 102206, PR China

ARTICLE INFO

ABSTRACT

In the present work, the hererostructured catalysts of g-C$_3$N$_4$/TiO$_2$ were synthesized and well characterized by XRD, SEM, TEM, Raman, UV–vis diffuse reflectance spectra, PL, Mott-Schottky, and XPS. Simultaneous photoreduction of Uranium(VI) and photooxidation of Arsenic(III) was firstly achieved over the g-C$_3$N$_4$/TiO$_2$ catalysts. And the experimental results show that the removal rate of U(VI) decreases with the increase of As(III) concentration, whereas the photooxidation rate of As(III) to As(V) increases with the increase of As(III) concentration. Noteworthily, the photoreduction of U(VI) to U(IV) and photooxidation of As(III) to As(V) was confirmed by XPS analysis in time-scale. The experimental results of free radical capture and quantitative test indicate that holes, hydroxyl radical and superoxide radical are the major active species for photooxidation of As (III), while U(VI) was reduced to U(IV) by the photogenerated electrons. Furthermore, a possible mechanism was proposed to well explain the improved photocatalytic performance of the g-C$_3$N$_4$/TiO$_2$ and the competitive relationship between photoreduction of U(VI) and photooxidation of As(III). The present work develops a heterostructured catalyst for potential application to the simultaneous removal of U(VI) and As(III), and makes clear the effect of photooxidation of As(III) on photoreduction of U(VI) for the first time.

1. Introduction

With the rapid development of modern industry, the shortage of fossil fuels and global warming became very seriously environmental and social issues [1]. Nuclear power, as a clean energy, has become increasing worldwide concerns because of without greenhouse gas emission. During the past several decades, anthropocentric activities, such as uranium mining [2] and processing [3], improper nuclear waste management and nuclear safety accidents, have resulted in the release of considerable amounts of uranium into the natural environment, mostly through migration in ground or surface water systems as the highly soluble uranyl (VI) ion [4,5]. Uranium's combination of chemotoxicity and radiotoxicity can lead to irreversible kidney damage, urinary system disease [6], DNA damage [7], and the disruption of biomolecules [8]. Meanwhile, the heavy metal pollution continues to undermine the environment of the whole earth, and endanger the human healthy and survival. Arsenium is commonly found in groundwater as well as industrial wastewater. It is highly toxic and known to

cause skin, lung, kidney, stomach and bladder cancers [9–11]. Furthermore, some literatures reported that arsenium contaminant will be associated during the uranium mining and utilization [12]. Thus, it is very urgent and meaningful to efficiently treat the wastewater containing uranium or arsenium [13].

Till now, several methods have been investigated to treat the uranium and arsenic wastewater. Hexavalent uranium (U(VI)) can be physically removed by solvent extraction [14], membrane filtration [15], and adsorption [16]. And U(VI) can be removed by chemical precipitation, chemical reduction [17] and biological treatment [18]. Meanwhile, the reported conventional methods for the removal of arsenium consist of adsorption [19], precipitation [20] and chemical oxidation [21]. These methods show some advantages for removing uranium and arsenium such as high adsorption capacity, rapid kinetics and high selectively [22,23]. However, due to the limited saturation of adsorption materials and the variety of surrounding environment, uranium pollution is likely to be returned to the aqueous system, leading to secondary pollution. Thus, it is necessary to develop new methods to

efficiently remove the trace amount of uranium or arsenium in the water.

Photocatalysis treatment technologies have been extensively studied to remediate contaminated water because they can well use sunlight and show good efficiency and environmental-friendly feature [24,25]. Recently, some researchers have reported that uranium and arsenium can be removed from aqueous solution over some photocatalysts under visible light or simulated sunlight irradiation. For example, Liu reported that U(VI) was reduced to U(IV) by B [26] or S [27] doped g-C_3N_4 under visible light irradiation. And TiO_2/Fe_3O_4 was used to remove U(VI) by the photocatalysis method [28]. Meanwhile, some catalysts were used to oxidize As(III) to As(V) under simulated sunlight irradiation, such as TiO_2 [29], Ferric Hydroxide [30] and Iron oxide nanoparticles [31]. However, the removal rate and efficiency of uranium and arsenium is still low and the quantum efficiency is very small because the photogenerated electrons and holes cannot be effectively used at the same time. And there are no reports on the combination of the simultaneous removal of uranium and arsenium by photocatalysis technology. In theory, the dual-purpose approaches of the coupling of the simultaneous removal of uranium and arsenium would be superior to the single-purpose ones in terms of efficiency and cost.

As well known, uranium species exist in several chemical states including U(III), U(IV), U(V), and U(VI), where the predominant chemical states are less soluble U(IV) and soluble U(VI). And the reduction potential of UO_2^{2+}/U^{4+}, UO_2^{2+}/UO_2 and U_4O_9/UO_2 is 0.267 V, 0.411 V and 0.456 V, respectively [32,33]. For arsenium, As(III) is the most prevalent form in the natural environment, which is more toxic than As(V) to environment, and As(III) is also more mobile than As(V). And the reduction potential of AsO_2/AsO_4^- and AsO_4^{3-}/AsO_2^- is 0.56 V and −0.71 V, respectively [34]. Thus the removal of soluble U(VI) was generally achieved by the reduction of U(VI) to less soluble U(IV), whereas the removal of As(III) was finished via the oxidation of As(III) to less toxic As(V) [35,36]. Furthermore, the photocatalysis technology contains photooxidation and photoreduction reactions. In order to efficiently remove U(VI) and As(III) in the water, it is desired to couple photoreduction of U(VI) with photooxidation of As(III) based on photocatalysis technology. Noteworthily, the combination of oxidation and reduction reactions would markedly improve the separation rate of photogenerated holes and electrons and enhance the quantum efficiency, leading to enhancement of removal rate of U(VI) and As(III).

To achieve the simultaneous and high-efficient removal of U(VI) and As(III) in the water, in this work, we firstly couple photoreduction of U(VI) with photooxidation of As(III) using the heterostructured catalyst of g-C_3N_4/TiO_2 under simulated sunlight irradiation. Furthermore, the photocatalytic improvement mechanisms of the heterostructured catalyst and the coupling mechanisms of simultaneous photoreduction of U(VI) and photooxidation of As(III) were systematically studied. And the results clearly indicate the enormous potential of the as-synthesized heterostructured catalyst in the treatment of radioactive and chemical toxic wastewater. The present work will pave the way for further developing high-efficient photocatalysis system for the simultaneous removal of uranium and arsenium.

2. Experiment section

2.1. Chemicals

All reagents were analytical grade and used without further purification. The detailed information of the chemicals are shown in the Supporting information (Text S1).

2.2. Syntheses

2.2.1. Synthesis of the mesoporous TiO_2

The mesoporous TiO_2 was synthesized via a modified solvothermal

process based on the previously reported method [37,38]. In a typical process, 0.1 mL of diethylenetriamine was added to 80 mL of isopropyl alcohol with vigorous stirring, and 3.8 mL of titanium isopropoxide was dropwised to the above solution under vigorous stirring. The mixture was stirred for 30 min and then transferred to a 100 mL Teflon-lined stainless-steel autoclave. After treatment at 200 °C for 24 h, a white precipitate was collected by centrifugation and washed with ethanol and deionized water several times. Finally, white powder of TiO_2 was obtained after dried at 120 °C for 4 h.

2.2.2. Synthesis of g-C_3N_4

Typically, 6.5 g of urea was put into an alumina crucible with a cover and then heated to 550 °C in a muffle furnace for 2 h at a heating rate of 8 °C min^{-1} based on the previously reported method [39]. After the reaction, the alumina crucible was cooled to room temperature, and a faint yellow powder of g-C_3N_4 was obtained.

2.2.3. Synthesis of g-C_3N_4/TiO_2 composites

The synthesis process of g-C_3N_4/TiO_2 composites was similar to that of the pure g-C_3N_4 via a calcination method [40]. A certain amount of urea (3.25, 6.5, 9.75, and 13 g) was mixed with the as-prepared TiO_2 (0.25 g), then the mixture was calcined under 550 °C in a muffle furnace for 2 h at a heating rate of 8 °C min^{-1}. After the reaction, the alumina crucible was cooled to room temperature, and a series of products with the color from white to yellow were obtained. The as-prepared g-C_3N_4/TiO_2 composites with mass ratio of g-C_3N_4 and TiO_2 being 20%, 40%, 60%, and 80% are denoted as 20 CNT, 40-CNT, 60-CNT, and 80-CNT, respectively.

2.3. Analyst methods

2.3.1. Measurement of As(III) concentration

The concentration of As(III) was measured using a hydride generation atomic fluorescence spectrometry (AFS-8220) equipped with an arsenic air cathode lamp. A citric acid-sodium citrate buffer solution (pH = 5) was used as the current-carrying liquid in the analysis. The signal of AsH_3 was recorded for the determination of arsenic concentration. Prior to analysis, the samples were diluted with the buffer solution to make sure the concentration of arsenic was lower than 10 μg/L. A solution composed of 2% KOH and 20% KBH_4 was employed as the reductant to reduce As(III) to AsH_3. Total arsenic was measured by mixing the sample solution with 1 mL of concentrated hydrochloric acid and 1 mL of thiocarbamide solution (5%) for 30–60 min to reduce As(V) to As(III). During this process, only As(III) could be converted to AsH_3.

2.3.2. Measurement of As(V) concentration

Molybdenum blue method was used to analyze the concentration of As(V). Typically, 6.5 g ammonium molybdate and 0.175 g antimony potassium tartrate were dispersed in 50 mL deionized water, and then added to 100 mL (v:v = 1:1) of sulfuric acid with deionized water under vigorous stirring to form solution A. 5 g ascorbic acid was dispersed in 50 mL deionized water to form solution B. Before the detection of the As(V) concentration, 1 mL solution B and 2 mL reagent A are successively added to a 40 mL sample aliquot in a 50 mL volumetric flask. A blank solution was prepared according to the same procedure using the appropriate volume of deionized water. The concentration of the As(V) was analysed by UV–vis spectrometry (MAPADA V-1100D) at wavelength of 870 nm.

2.3.3. Measurement of U(VI) concentration

Arsenazo-III method was used to analyze U(VI) concentration. Solution A of 0.1% 2,4-dinitrophenol, solution B of 3 mol/L hydrochloric acid, solution C of chloroacetic acid-sodium acetate buffer solution, and solution D of 0.5 g/L arsenazo-III were prepared. Then the solutions A–D (according to the volume ratio of (1:3:4:4)) were mixed.
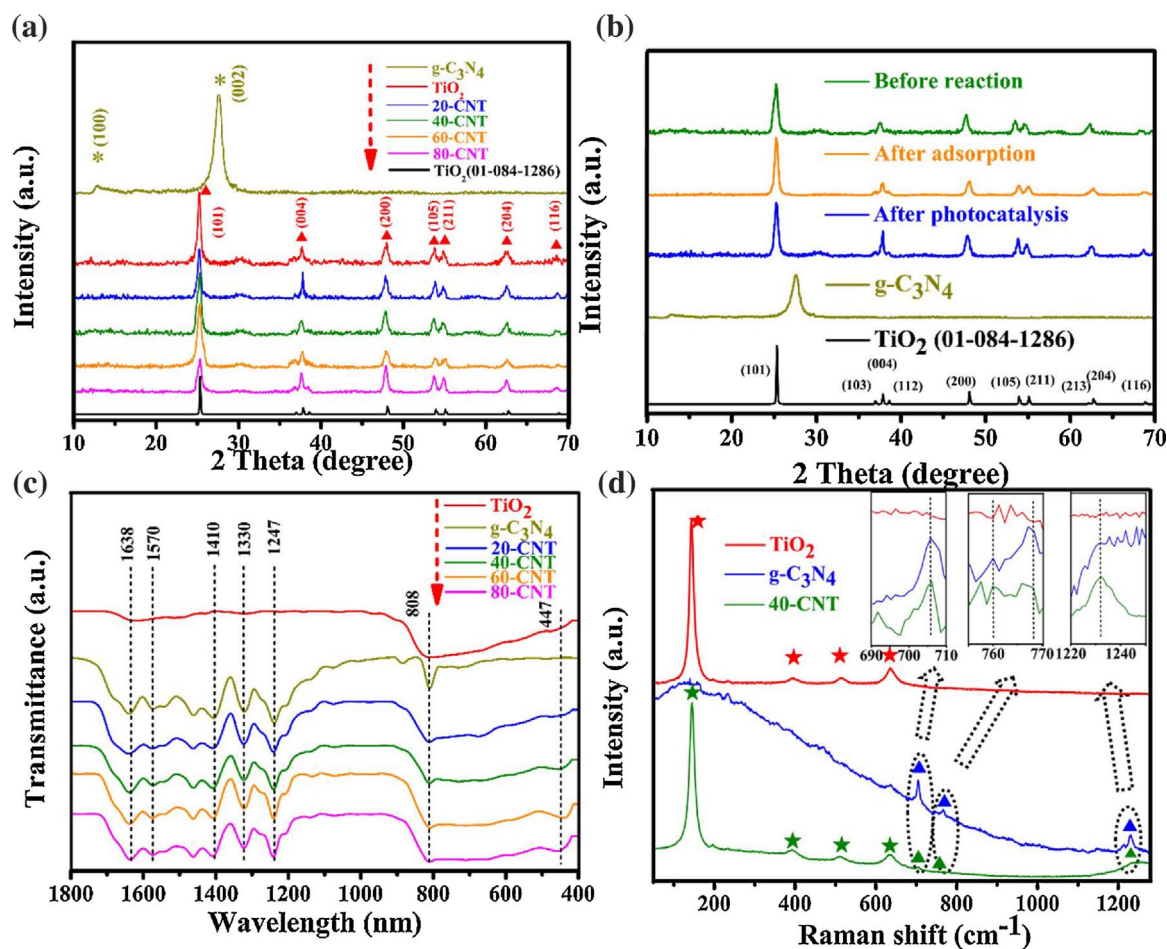
Fig. 1. XRD of the g-C$_3$N$_4$, TiO$_2$ and g-C$_3$N$_4$/TiO$_2$ composites with different loading amount of g-C$_3$N$_4$ (a) and the 40-CNT before reaction and after 4h photocatalytic reaction (b). FT-IR spectra (c) and Raman spectra (d) of the as-prepared samples.

The concentration of the U(VI) was analyzed by UV–vis spectrometry (MAPADA V-1100D) at wavelength of 652 nm.

2.4. Characterizations

The crystalline phases of samples were identified by X-ray diffraction (Bruker D8 ADVANCE) by using graphite-monochromatized Cu Kα (λ = 1.5406 Å) radiation. The morphology of samples was observed with scanning electron microscopy (SEM) and transmission electron microscopy (TEM). Composition analyses on the as-prepared catalysts were carried out on a field-emission scanning electron microscope equipped with energy dispersive X-ray spectroscopy (EDS). UV–vis diffuse reflectance spectra (DRS) were recorded with a PE Lambda 900 UV/vis spectrophotometer at room temperature. X-ray photoelectron spectroscopy (XPS) measurements were taken by using a VG Escalab 250 spectrometer equipped with an Al anode (Kα = 1486.7 eV). Brunauer-Emmett-Teller (BET) surface areas of samples were measured by means of N$_2$ adsorption over a NOVA2000e (Quantachrome) equipment. Raman spectra were recorded on a Renishaw Raman spectrometer with 785 nm laser at a power of 4.7 mW.

Electrochemical measurement was carried out on an Electrochemical Station CHI 660D. In the three-electrode system, a graphite counter electrode and a standard calomel reference electrode in saturated KCl were used. The working electrodes were prepared by dip-coating. The details are shown below: 50 mg of photocatalyst was suspended in 5 mL of deionization water to produce a slurry that was then dip-coated onto a 1 cm × 1 cm fluorine-tin oxide (FTO) glass electrode. After dried under ambient conditions, the films were sintered

at 300 °C for 1 h. Prior to and during all measurements, the electrolyte (0.5 M Na$_2$SO$_4$) was purged with nitrogen. For photocurrent measurements, a 300 W Xe lamp was used as the source of simulated sunlight irradiation, and the other conditions were similar to those of electrochemical measurements. The flat band potentials (V$_{fb}$) were electrochemically determined from Mott-Schottky plots. The fluorescence spectra were measured by Hitachi F-7000 fluorescence spectrometer (Japan) with the maximum excitation wavelength of 325 nm.

2.5. Photocatalytic reaction

Experiments were conducted in a 100 mL photoreactor cooled by circulation water (20 ± 2 °C). During each experiment, 25 mg of catalysts were suspended in a 100 mL solution containing U(VI) (20 mg/L) and As(III) (20 mg/L). The pH was adjusted by using H$_2$SO$_4$ (0.1 M) or NaOH solutions (0.1 M). The solution was magnetically stirred in dark for 2 h to reach the adsorption-desorption equilibrium of U(VI) and As (III) on the surface of photocatalyst. A 300 W Xe lamp (wavelength range 320 nm ≤ λ ≤ 780 nm, light intensity 160 m W/cm^2) was used as the source of simulated sunlight. At given times, aliquot (2 mL) of the solution were pipetted and filtered through 0.45 μm Nylon syringe filters. The clean liquid was analyzed by atomic fluorescence spectrophotometer (AFS-8220) to determine the concentration of As(III). Argon (99.99%) was used as carrier gas and shielding gas during the determination. The concentration of As(V) was measured by spectra photometrically (MAPADA V-1100D) using the molybdenum blue method. And the concentration of UO$_2^{2+}$ was analyzed by UV–vis spectrometry with arsenazo-III as the chromogenic agent at wavelength

of 652 nm [41,42]. All tests were performed in duplicate and results were averaged. Removal rate (%) of uranium and arsenium by photocatalysts in solution were defined as removal rate (%) = C_t/C_0, where C_0 and C_t are the concentration (mg/L) of uranium and arsenium at initial and contact time t (min), respectively.

2.6. Quantification of superoxide radicals and hydroxyl radicals

In the photocatalytic process, nitroblue tetrazolium (NBT) transformation and terephthalic acid (TA) were used as probe compounds to indicated the variations in the formation rates of $\cdot O_2^-$ and $\cdot OH$ with different times at pH = 6.9, respectively. By recording the concentration of NBT on a UV–vis spectrophotometer, the production of $\cdot O_2^-$ was quantitatively analyzed. Upon combining with $\cdot OH$, TA was transformed into a highly fluorescent product of 2-hydroxyterephthalic acid. The production of $\cdot OH$ was quantitatively resolved by monitoring the PL intensity of 2-hydroxyterephthalic acid (excitation at 315 nm) [43–45].

3. Results and discussion

3.1. Characterizations of the as-prepared samples

As shown in Fig. 1a, the as-prepared samples of g-C_3N_4, TiO_2 and g-C_3N_4/TiO_2 composites display good crystallinity. g-C_3N_4 nanosheets have two main diffraction peaks at 2θ = 27.8° and 13.1°, corresponding to (0 0 2) and (1 0 0) plane of g-C_3N_4, respectively. The diffraction peaks of TiO_2 were consistent with the standard card (JCPDS 01-084-1286) of the anatase TiO_2. The diffraction peaks with 2θ values of 25.2°, 37.8°, 47.9°, 53.9° and 62.6° correspond to the (1 0 1), (0 0 4), (2 0 0), (1 0 5), and (2 0 4) crystal faces of the anatase TiO_2, respectively. For the g-C_3N_4/TiO_2 composites, when the loading amount of g-C_3N_4 in the g-C_3N_4/TiO_2 composites increases from 0 to 80%, the characteristic peaks of g-C_3N_4 still cannot be clearly observed in the XRD pattern. It could be due to the peaks' intensities of TiO_2 showing much stronger than that of g-C_3N_4. In addition, as shown in Fig. 1b, the 40% g-C_3N_4/TiO_2 (40-CNT) composite became unchanged after 2 h photoreaction, indicating that the 40-CNT catalyst has good stability. As shown in Fig. 1c, the g-C_3N_4 exhibits typical band at 808 cm^{-1}, corresponding to the breathing mode of the heptazine arrangement (N=N of the tetrazine ring), while the adsorption band at 1638 cm^{-1} can be ascribed to the C−N heterocycle stretching vibration modes. And the four strong peaks at 1570, 1410, 1330, and 1247 cm^{-1} are assigned to aromatic C−N stretching vibration modes. The pure TiO_2 shows two weak absorption peaks at 3403 and 1608 cm^{-1}, corresponding to the stretching vibration and bending vibration absorption peak of –OH from a small quantity of H_2O absorbed by TiO_2, whereas the strong absorption at 600 cm^{-1} is ascribed to the bonds of Ti−O and Ti−O−Ti. For the CNT composites, the main characteristic peaks of TiO_2 and g-C_3N_4 appear in the CNT composites, suggesting both TiO_2 and g-C_3N_4 exist in the as-prepared composites. In order to confirm the existence of g-C_3N_4 sheets in the CNT composites, Raman spectra were also investigated. As shown in Fig. 1d, several weak characteristic peaks at 320, 474, 702, 746, 980, and 1225 cm^{-1} were observed in the g-C_3N_4. For pure TiO_2, the peaks at 146 cm^{-1} (E_g), 399 cm^{-1} (B_{1g}), 516 cm^{-1} (A_{1g}), and 640 cm^{-1} (E_g) can be attributed to the characteristic peaks of the anatase phase [46]. And these characteristic peaks are also observed in the 40-CNT composites, indicating both TiO_2 and g-C_3N_4 exist in the 40-CNT composite. Moreover, the characteristic peaks of the g-C_3N_4 (320 and 474 cm^{-1}) have a little shift after the introduction of TiO_2, showing that good contacts between TiO_2 and g-C_3N_4 were formed, which is beneficial to the separation of photogenerated charges.

The morphology and microstructure of as-prepared samples were investigated by SEM, TEM and EDS. As shown in Fig. 2a and b, the as-synthesized g-C_3N_4/TiO_2 composites were composed of a large number of hierarchical microspheres of TiO_2 and a flat layer of g-C_3N_4. Besides,

TEM images of the g-C_3N_4/TiO_2 also confirm the hollow-shell structure of TiO_2 and thin smooth and flat layers of g-C_3N_4 in the g-C_3N_4/TiO_2 composites (Fig. 2c and d). HRTEM of the 40-CNT in Fig. 2e and f reveal that the lattice fringe spacing of 0.351 nm and 0.336 nm correspond to the (1 0 1) crystal plane of g-C_3N_4 and the (0 0 2) crystal plane of TiO_2, respectively. And the EDS pattern in Fig. 2g and h indicate that the 40-CNT composites contain C, N, Ti and O elements, confirming the existence of g-C_3N_4 and TiO_2 in the g-C_3N_4/TiO_2 composites. These results indicated that the g-C_3N_4/TiO_2 composite catalysts are composed of novel hollow-shell structure of TiO_2 and thin smooth and flat layers of g-C_3N_4. And TEM images confirm that g-C_3N_4 and TiO_2 were successfully coupled in the g-C_3N_4/TiO_2 composites to form heterostructure.

In order to investigate the composition and the chemical bonding environment of the as-prepared samples, X-ray photoemission spectroscopy (XPS) was carried out. As shown in Fig. 3a, three peaks were obtained after deconvolution in the high-resolution XPS spectrum of C 1s for g-C_3N_4. The peak at 284.52 eV was assigned to the adventitious carbon, whereas the peaks at 285.90 eV and 287.77 eV were assigned to the C=N groups and C−N (or C−(N)$_3$) groups, respectively. The C 1s spectrum for 40-CNT was similar to that of the g-C_3N_4, but the peaks' positions of the C=N and C−N (or C−(N)$_3$) have a shift of 0.32 eV and 0.51 eV towards higher binding energy. In the N 1s spectrum of g-C_3N_4 in Fig. 3b, peaks at 398.21, 399.21 and 401.77 eV could be assigned to sp^2-hybridized aromatic N (C=N−C), tertiary nitrogen N−(C)$_3$ and C−N−H groups, respectively [47]. Compared with the peaks in g-C_3N_4, those three peaks of the 40-CNT shift to 0.89, 1.2 and 0.26 eV towards higher binding energy, respectively, which could be attributed to the chemical environment change arising from the close contact between g-C_3N_4 and TiO_2 to form heterostructure. As can be seen in Fig. 3c, three peaks can be observed at 531.08, 531.87 and 532.84 eV, which could be assigned to "O_2^{-}" ions in the lattice, adsorbed OH$^-$ species and O$^-$ species (or oxygen vacancies and molecular water), respectively [48]. And peaks at 457.73 and 463.45 eV can be assigned to Ti 2p$_{3/2}$ and Ti 2p$_{1/2}$, respectively (Fig. 3d), indicating the Ti^{4+} in the g-C_3N_4/TiO_2 composites. The results confirm the successful formation of heterostructure in the g-C_3N_4/TiO_2 composites.

As shown in Fig. 4a, the g-C_3N_4/TiO_2 composite exhibit much higher absorption intensity than that of the g-C_3N_4 and TiO_2, and the adsorption edge of the g-C_3N_4/TiO_2 composite red-shifts in comparison with that of the g-C_3N_4 and TiO_2, showing the g-C_3N_4/TiO_2 composite have better light adsorption performance than the g-C_3N_4 and TiO_2. Compared with g-C_3N_4, the PL peak intensity of the 40-CNT was much lesser (Fig. 4b), showing that the 40-CNT exhibits lower recombination rate of photogenerated electrons and holes. Meanwhile, the photocurrent measurements were carried out over the as-prepared samples deposited on FTO electrodes at bias potential of 0.24 V. The 40-CNT exhibits the largest intensity of fast photocurrent responses among the as-prepared samples (Fig. 4c). And electrochemical impedance spectrum (EIS) of the 40-CNT shows the smallest semicircle among the as-prepared samples (Fig. 4d), confirming that the 40-CNT exhibits more efficient charge separation, leading to much better photocatalytic performance than the g-C_3N_4 and TiO_2.

3.2. Simultaneous photocatalytic removal of U(VI) and As(III) by g-C_3N_4/TiO_2

Fig. 5a shows the removal efficiencies of U(VI) and As(III) by the g-C_3N_4/TiO_2 composite, TiO_2 and g-C_3N_4 in a solution containing 20 mg/L of U(VI) and 20 mg/L of As(III) solution at pH = 6.9. No changes in U(VI) and As(III) concentration were observed under irradiation in the absence of photocatalyst. Under simulated sunlight irradiation, the concentration of U(VI) and As(III) in the solution rapidly decrease over the catalyst, whereas the concentration of As(V) in the solution gradually increases. Among the as-prepared catalysts, the 40-CNT shows the best photocatalytic performance of U(VI) reduction and As(III) oxidation. After 4 h photocatalytic reaction, about 83% of U(VI) and
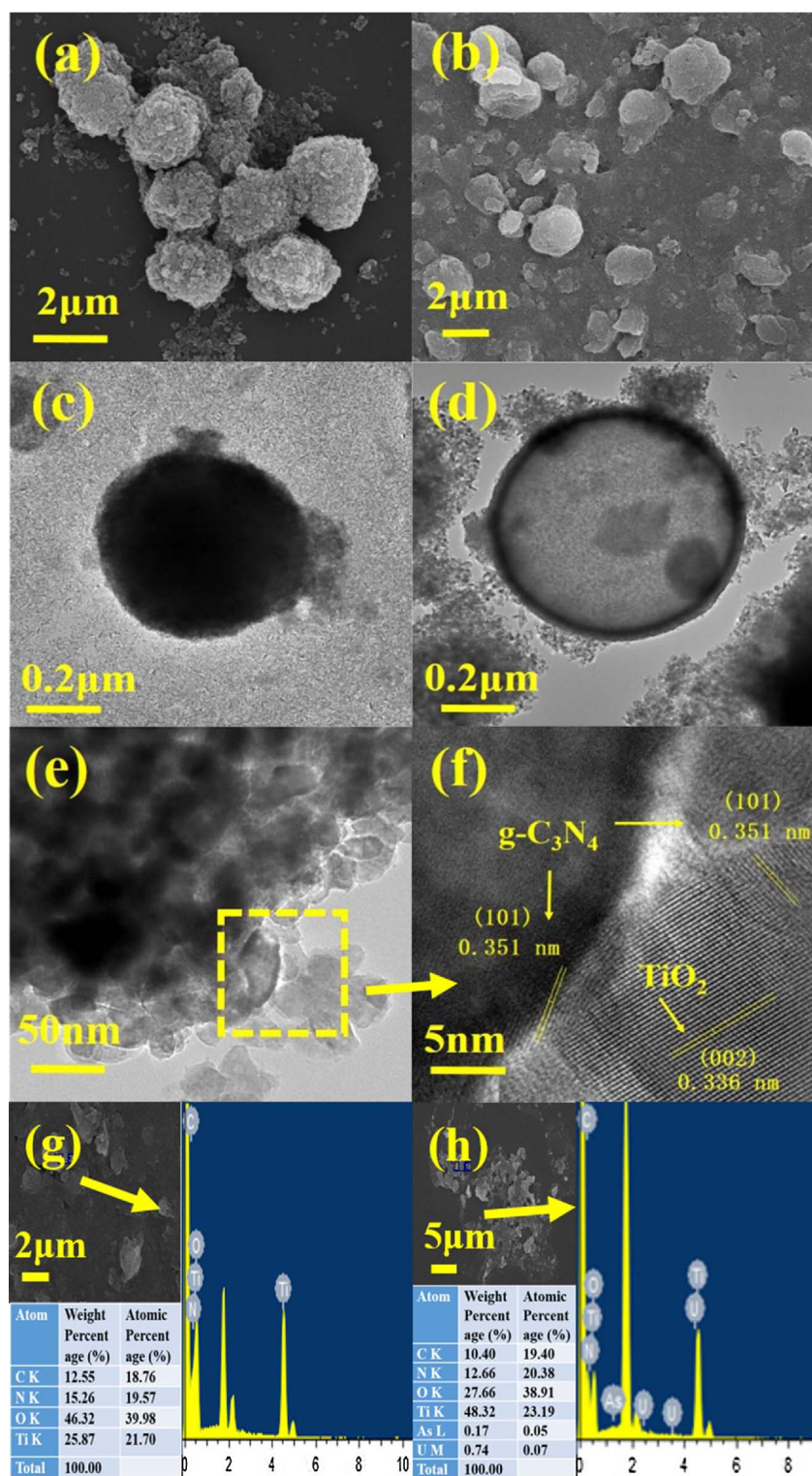
Fig. 2. SEM images of TiO₂ (a) and 40-CNT (b); TEM images of TiO₂ (c) and 40-CNT (d); HRTEM images of 40-CNT (e) and (f), EDS images on 40-CNT before reaction (g) and after reaction (h).

Table (g):

Atom	Weight Percentage (%)	Atomic Percentage (%)
C K	12.55	18.76
N K	15.26	19.57
O K	46.32	39.98
Ti K	25.87	21.70
Total	100.00	

Table (h):

Atom	Weight Percentage (%)	Atomic Percentage (%)
C K	10.40	19.40
N K	12.66	20.38
O K	27.66	38.91
Ti K	48.32	23.19
As L	0.17	0.05
U M	0.74	0.07
Total	100.00	

40% of As(III) was removed by the catalyst of 40-CNT, while the concentration of As(V) increase from 0 to 8.4 mg/L. Besides, we can clearly observed the U(VI) concentration was declined and As(III) was rised in the reaction by UV–vis absorption spectra in Fig. S1. As a comparison, the g-C₃N₄, TiO₂ and the physical mixture of TiO₂ and g-C₃N₄ has much lower photocatalytic activity of U(VI) photoreduction and As(III) photooxidation than that of the 40-CNT.

3.3. Effects of the different proportions of U(VI) and As(III) concentration

As shown in Fig. 5b and S2, the removal rate of U(VI) and As(III) are 67.02% and 36.91% over the 40-CNT in the single solution of U(VI) (20 mg/L) and As(III) (20 mg/L), respectively. As a comparison, the removal rate of U(VI) and As(III) increases to 82.66% and 41.18% in the mixed solution of U(VI) (20 mg/L) and As(III) (20 mg/L), respectively. The results indicate that the 40-CNT heterocontructured catalyst possesses excellent synergistic effect on the removal of the U(VI) and As
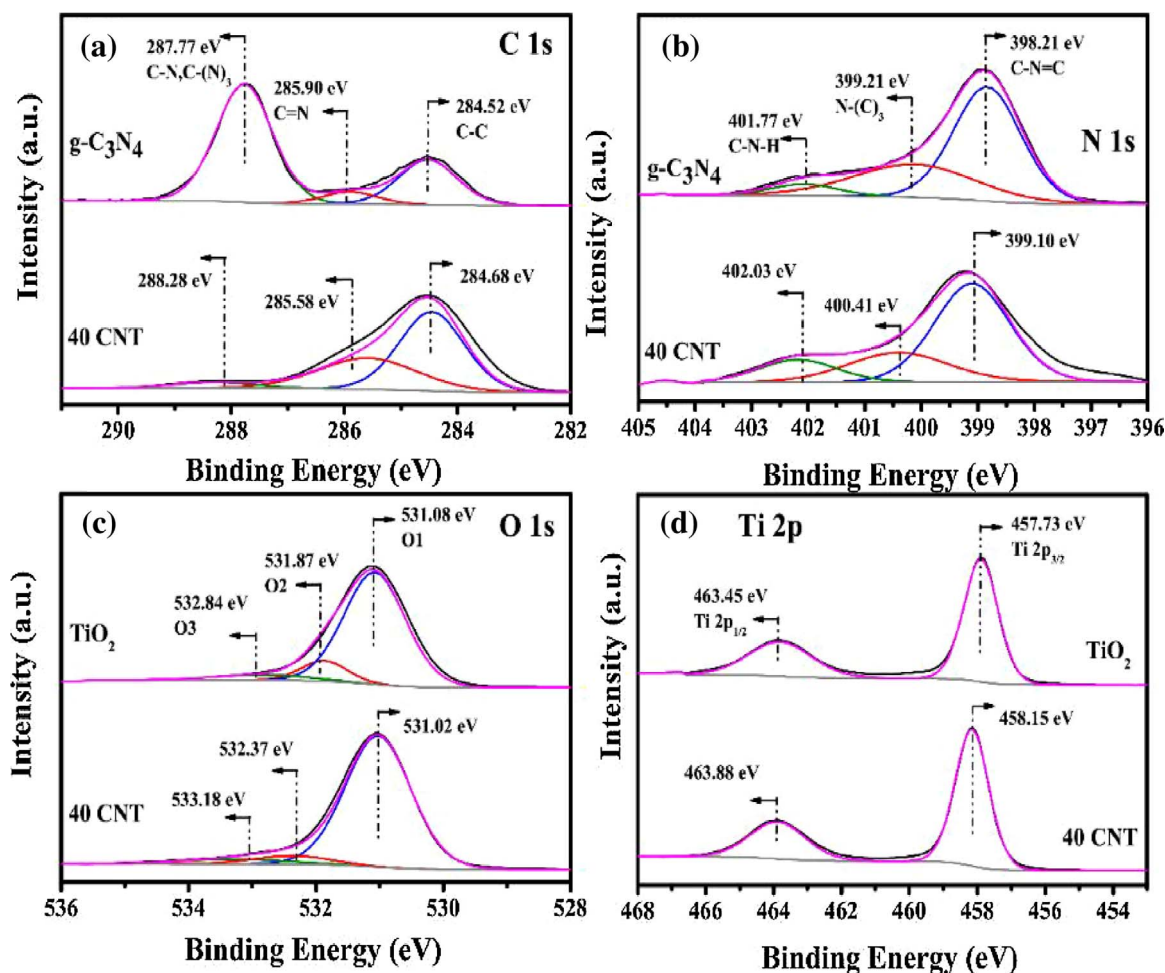
Fig. 3. XPS spectra for C 1s (a), N 1s (b), O 1s (c), and Ti 2p (d) of the TiO_2, $g-C_3N_4$ and 40-CNT.

(III). Moreover, to further investigate the effect of As(III) concentration on U(VI) removal, As(III) concentration changes from 20 mg/L to 60 mg/L. When U(VI):As(III) = 1:2, the removal rate of U(VI) decreases to 62.55%, whereas the removal rate of U(VI) are 55.73% when U (VI):As(III) = 1:3. For As(III) oxidation, with the increase of As(III) concentration from 20 mg/L to 60 mg/L, the removal amount of As(III) increases from 8.23 mg/L to 9.66 mg/L and the formation amount of As (V) increases from 8.2 mg/L to 9.4 mg/L, accordingly. The results indicate the removal rate of U(VI) decreases with the increase of As(III) concentration, whereas the photooxidation rate of As(III) to As(V) increases with the increase of As(III) concentration, which could be due to some photogenerated electrons are used for the oxidation of As(III) to As(V).

3.4. Effects of co-existing ions

The general cations (e.g., Na^+, K^+, Mg^{2+}, etc.) and anions (e.g., NO_3^-, Cl^-, etc.) are widespread in the seawater and industrial wastewater [49,50]. These components would influence the speciation and migration of the target metal ions due to their different affinity for binding on the solid surfaces. The photocatalytic experiments were conducted in the solution containing 0.01 mol/L of NaX (herein, X = NO_3^- and Cl^-), 0.01 mol/L of $MgNO_3$ and 0.01 mol/L of MCl (herein, M = Na^+ and K^+) at pH values of 6.9. As shown in Fig. 6a is drawn by the mean value in Table S2, compared with the removal rate of U(VI) and As(III) in the deionized water, the photocatalytic removal rate of U(VI) and As(III) were slightly decrease from 48.03% to 40.21% and 29.86% to 28.58%, respectively, in the mixed solution of NaX,

$MgNO_3$ and MCl. And the formation rate of As(V) was nearly constant in the two different solution systems. Besides U(VI) and As(III), other ionic concentration was also measured by AAS (Atomic Absorption Spectrometry). As shown in Fig. S3, the concentration of Na^+, K^+ and Mg^{2+} nearly became unchanged, whereas that of NO_3^- and Cl^- slightly decreased due to the weak complexing affinity of NO_3^- and Cl^- with $(UO_2)_3(OH)_5^+$ [51]. The above results indicate that the co-existing ions have little effect on the photocatalytic removal of U(VI) and As(III) over the 40-CNT.

3.5. Reusability of catalysts and practical application

The stability of the 40-CNT was investigated by a five-run cycle test of photocatalytic reduction of U(VI) coupled with simultaneous oxidation of As(III). After every cycle run, the photocatalysts were collected and washed with 1 mol/L HNO_3 solution and 1 mol/L NaOH solution to remove the U(VI) and As(III) deposited on the surface of 40-CNT, and then washed by the deionized water. Afterward, the photocatalysts were dried by in vacuum at 60 °C for 6 h for the next cycle reaction. As shown in Fig. 6b and c are drawn by the mean value in Table S3, after five cycle runs, the U(VI) removal rate decrease from 48.03% to 41.33%, while the As(III) removal rate decrease from 29.86% to 28.66% under simulated sunlight. The results prove that the heterostructured catalyst of 40-CNT exhibits good stability for the simultaneous photocatalytic removal U(VI) and As(III).

In addition, the as-synthesized 40-CNT catalyst was used to the removal of U(VI) and As(III) in the actual lake water. The real waste lake water was collected from Tianyi lake, Jiangxi Province, China (located
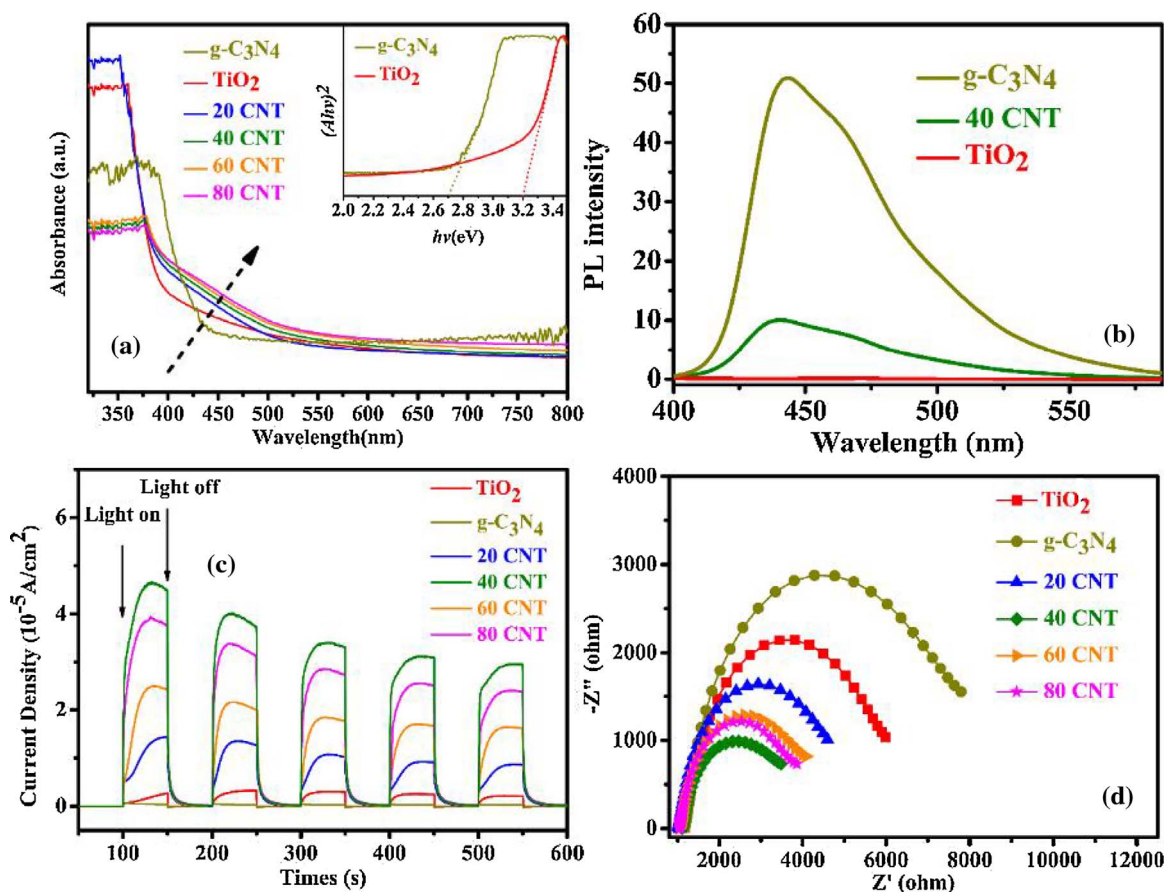
Fig. 4. Diffuse reflectance spectroscopy (a), PL spectra (b), Transient photocurrent responses (c) and EIS curves (d).

in 28°38′52″N, 115°49′52″E) (details of the kinds and concentration of pollutants was mentioned in Table S1 in SI). Concentrated U(VI) and As (III) solution was added to the above lake water to make the U(VI) and As(III) concentration of the lake water reaching 5 mg/L. As shown in Fig. 6d, U(VI) can be nearly cleaned up, whereas the residual As(III) concentration and the generated As(V) concentration is 1.06 mg/L and 1.09 mg/L (as shown in Fig. S4) after 4 h photocatalytic reaction, which meets to the national emission standard with U(VI). These results indicated that the heterostructured catalyst of 40-CNT can be applied by the actual wastewater treatment of U(VI).

3.6. Photocatalytic mechanism of simultaneous removal of U(VI) and As (III)

To further investigate the photocatalytic mechanism, free radicals species in the photocatalytic process were detected. t-BuOH (TBA), EDTA$_2$Na and BQ were introduced as scavengers of hydroxyl radical (·OH), hole (h^+) and superoxide radical (·O$_2^-$), respectively. As shown in Figs. 7a and S5, the removal of the U(VI) becomes nearly unchanged with the addition of t-BuOH (TBA), EDTA$_2$Na or BQ. The removal rate of As(III) decreases from 41.176% to 28.441% in the presence of BQ, whereas the removal rate of As(III) declines to 31.684% and 34.465%
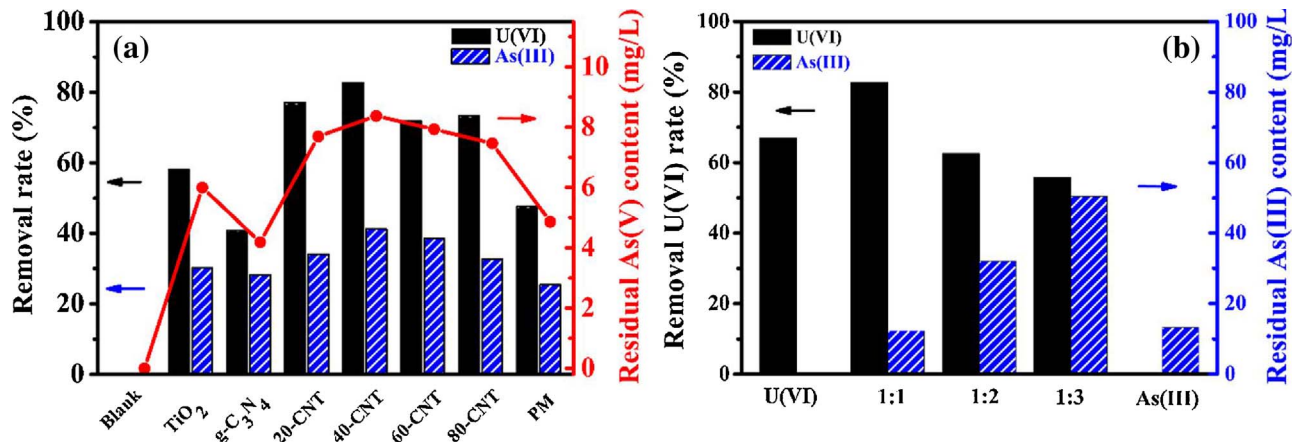

Fig. 5. (a) Removal rate of U(VI) and As(III) and the transformation amount of As(V) from As(III) in the solution over the as-prepared photocatalysts. (PM means the physical mixture of 40 wt.% g-C$_3$N$_4$ and TiO$_2$) (b) Removal rate of U(VI) and formation amount of As(V) in different proportions of U(VI) concentration and As(III) concentration with 1:1, 1:2 and 1:3. Conditions: M(catalysts) = 25 mg, V = 100 mL, C$_0$(U(VI)) = 20 mg/L, C$_0$(As(III)) = 20, 40 and 60 mg/L, and pH = 6.9.
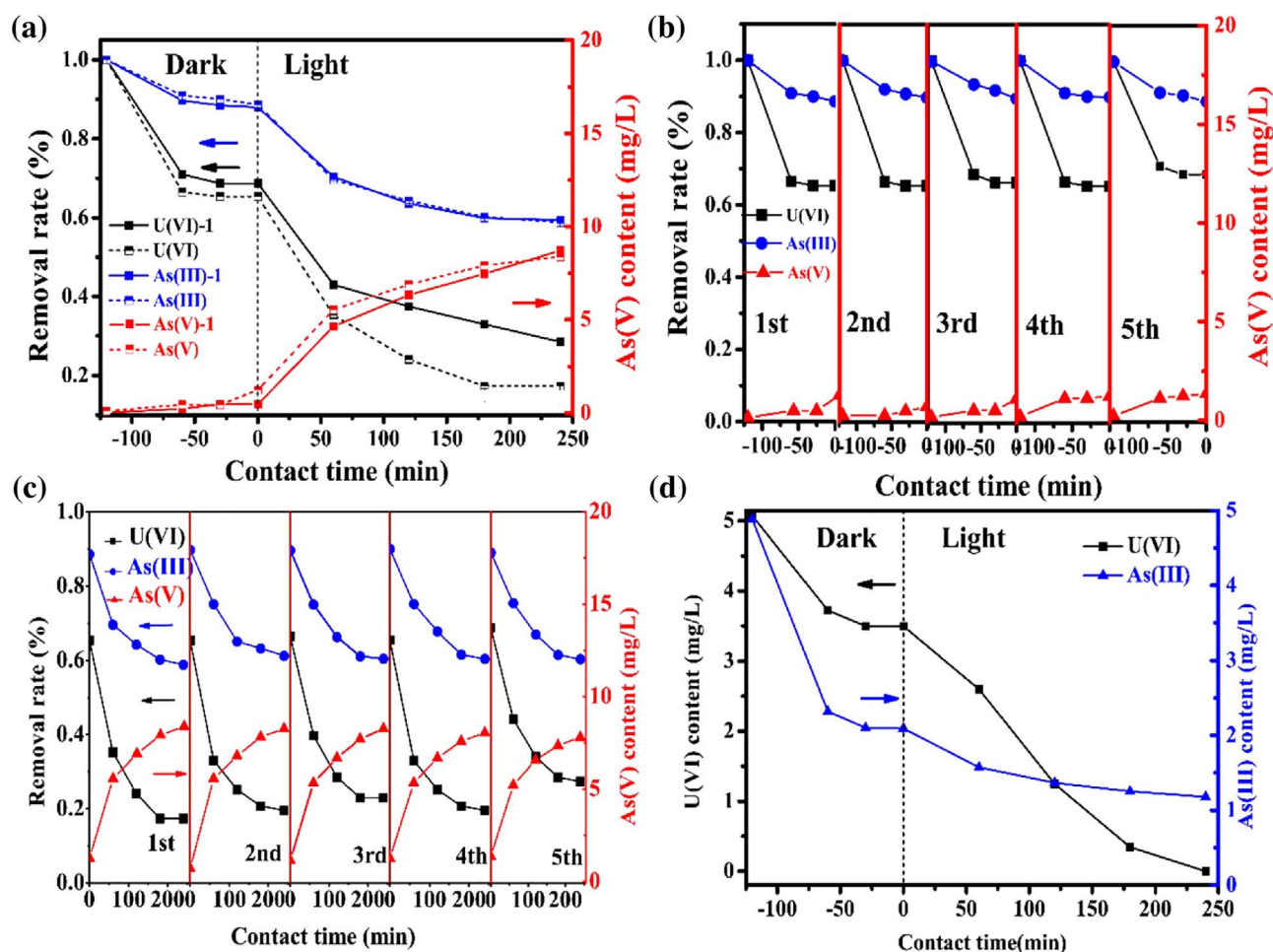
Fig. 6. Removal rate of U(VI) and As(III), and the generated amount of As(V) from As(III) over the 40-CNT in deionized water and in the presence of co-existing ions under simulated sunlight irradiation (U(VI)-1, As(III)-1 and As(V)-1 represent the results in deionized water. Conditions: M(catalysts) = 25 mg, V = 100 mL, C_0(U(VI)) = 20 mg/L, C_0(As(III)) = 20 mg/L, and pH = 6.9.) (a). Cycling runs of simultaneous removal of U(VI) and As(III) over the 40-CNT by dark adsorption (b) and under simulated sunlight irradiation (c) for 20 h. The removal of U(VI) and As(III) in the natural lake water over the 40-CNT under simulated sunlight irradiation for 4 h (d).
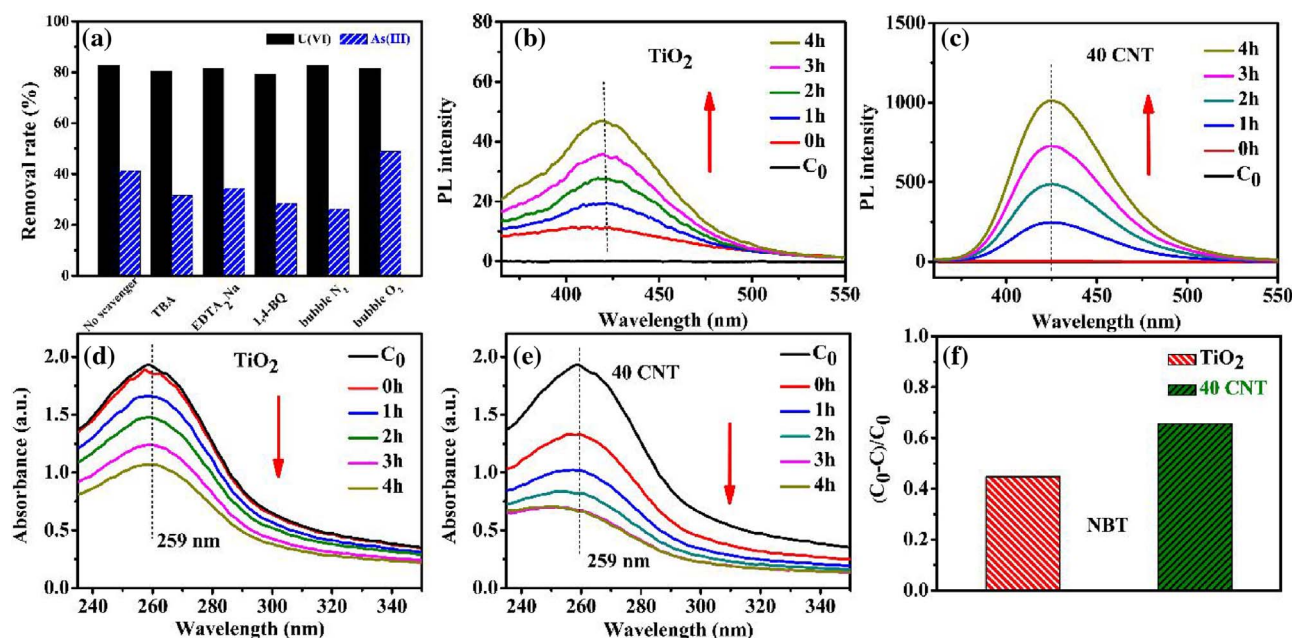
Fig. 7. Influence of various scavengers on the photocatalytic activity of the 40-CNT in the U(VI) and As(III) solution (a); Fluorescence intensities of hydroxyterephthalic acid (TAOH) catalyzed by the TiO₂ (b) and 40-CNT (c); Time-resolved absorption spectra of NBT catalyzed by the TiO₂ (d) and 40-CNT (e); Transformation efficiency of NBT catalyzed by the TiO₂ and 40-CNT (f).

with the addition of TBA and EDTA$_2$Na, respectively. The results reveal that ·OH, h^+ and ·O$_2^-$ act as the main reactive species in the As(III) photooxidation reaction. When N$_2$ was bubbled into the reaction system, the removal rate of As(III) was markedly inhibited from 41.176% to 26.249%, whereas the removal rate of As(III) enhances from 41.176% to 48.919% with bubble of O$_2$ (Fig. 7a). This result indicates that molecular oxygen has important effect on the photooxidation As(III) over 40-CNT.

The terephthalic acid photoluminescence technique (TA-PL) was used to estimate the amount of ·OH radicals formed during photocatalysis. Terephthalic acid (TA) reacts with ·OH radicals to form the highly fluorescence 2-hydroxy terephthalic acid (TAOH) that has a photoluminescence signal at around 425 nm [52]. As shown in Fig. 6b and c, the 40-CNT composite shows obvious higher PL intensity than TiO$_2$, suggesting that heterostructured catalyst produces more ·OH radicals than TiO$_2$, in consistent with the experimental results of radicals' scavenger. In addition, nitroblue tetrazolium (NBT) transformation experiments were carried out to quantitatively detect the amount of ·O$_2^-$ radical generated during the photocatalytic reaction. As shown in Fig. 7d and e, the absorbance intensity of NBT (at wavelength 259 nm) catalyzed by TiO$_2$ and 40-CNT decreases from 1.931 to 1.068 and 0.664, respectively, showing the NBT conversion percentage over the 40-CNT is up to 65.61%, much larger than that over the TiO$_2$ of 44.69% in Fig. 7f. The results suggest the 40-CNT can more easily produce ·O$_2^-$ than the TiO$_2$.

3.7. XPS analysis

To deeply elucidate interaction mechanisms between U(VI), As(III) and the photocatalysts, the 40-CNT sample after the reaction with U(VI) (20 mg/L) and As(III) (20 mg/L) at pH 6.9 condition were characterized by means of XPS.

XPS spectra of the 40-CNT with different reaction time were presented in Fig. 8. As shown in Fig. 8a, two obvious peaks at 392.20 and 381.24 eV are assigned to the U 4f$_{5/2}$ and U 4f$_{7/2}$ of U(VI), respectively. The existence of U(VI) before photocatalytic reaction could be due to some UO$_2$(OH)$_2$·H$_2$O adsorbed on the surface of the 40-CNT (0 h). After 1 h reaction, two peaks at 390.91 and 379.84 eV were founded, which are ascribed to the U 4f$_{5/2}$ and U 4f$_{7/2}$ of U(IV), respectively, confirming

Fig. 8. XPS spectra of U(VI) and As(III) over the 40-CNT at the different reaction time.

the formation of UO$_2$. And the intensities of the two peaks at 390.90 ± 0.2 eV and 379.90 ± 0.1 eV (U(IV)) increase from 25.69% to 51.62% with increase of reaction time from 1 to 4 h, whereas the peaks' intensities of the U 4f$_{5/2}$ and U 4f$_{7/2}$ of U(VI) (392.20 ± 0.1 eV and 381.30 ± 0.1 eV) decrease from 74.31% to 48.38% with increase of reaction time from 1 to 4 h. The results confirm that the amount of UO$_2$ was gradually generated, whereas the amount of UO$_2$(OH)$_2$·H$_2$O were gradually consumed during the process of U(VI) removal using 40-CNT. As shown in Fig. 8b, the peaks at 43.88 eV can be attributed to the As 3d of As(III). With the increase of reaction time from 1 to 4 h, the peak's intensity of As(III) decreases from 81.90% to 58.82%, whereas that of As(V) increases from 18.10% to 41.18% (the detail data are shown in Table S4). The above results indicate U(VI) and As(III) were absorbed on the surface of the 40-CNT sample, and then U(VI) was reduced to U(IV), while As(III) was oxidized to As(V).

3.8. Photocatalytic enhancement mechanism

As shows in Fig. S6, the V$_{fb}$ is calculated to be −0.49 V and −0.45 V vs SCE for g-C$_3$N$_4$ and TiO$_2$, respectively (equivalent to −0.25 V and −0.21 V vs NHE, respectively). Because the flat band potential of n-type semiconductor equals the Fermi level (EF), the EF values of g-C$_3$N$_4$ and TiO$_2$ are −0.25 V and −0.21 V. Accordingly, the CB of g-C$_3$N$_4$ and TiO$_2$ is −0.45 and −0.41 V vs NHE, respectively. The VB of g-C$_3$N$_4$ and TiO$_2$ can be calculated as 2.24 V and 2.79 V, respectively.

As shown in Scheme 1, under simulated sunlight irradiation, electrons (e^-) in VB are excited to CB, with the same amount of holes (h^+) left in VB of g-C$_3$N$_4$ and TiO$_2$. Then, electrons in the CB of g-C$_3$N$_4$ flow into the CB of TiO$_2$ because the former is more negative than the latter. In the meantime, the photogenerated holes in the VB of TiO$_2$ flow into the VB of g-C$_3$N$_4$ because the VB of TiO$_2$ is more negative than that of g-C$_3$N$_4$. The photogenerated holes in the VB of g-C$_3$N$_4$ can react with OH- to yield ·OH because the VB potential of g-C$_3$N$_4$ (+2.24 V) is more positive than E° (·OH/H$_2$O) (+1.99 V vs NHE) at the pH of 6.9 in the reaction condition. And some photogenerated electrons in the CB of TiO$_2$ can react with O$_2$ to yield ·O$_2^-$ because the CB potential of TiO$_2$ (−0.41 V) is more negative than E° (O$_2$/·O$_2$-) (−0.046 V vs NHE). Finally, the generated hydroxyl radicals, superoxide radical and some photogenerated holes oxidize As(III) to As(V), in consistent with the above photocatalytic results. For U(VI) reduction, some photogenerated electrons in the CB of TiO$_2$ can directly react with U(VI) to form U(IV). Because both reduction of U(VI) and oxidation of As(III) consume photogenerated electrons, the two photocatalytic processes compete with each other, which explains why the removal rate of U(VI) decreases with the increase of As(III) concentration (Scheme Scheme 11).

4. Conclusions

This paper reported that g-C$_3$N$_4$/TiO$_2$ composite catalysts were synthesized by a facile method of combination of hydrothermal and calcination method. The characterizations of XRD, SEM, TEM, Raman, UV–vis diffuse reflectance spectra, PL, Mott-Schottky, and XPS were done to confirm the heterostructured g-C$_3$N$_4$/TiO$_2$ catalysts. Experimental results show that the 40-CNT sample exhibits the highest photocatalytic performance for the simultaneous photoreduction of U (VI) and photooxidation of As(III) among the as-prepared catalysts. And the removal rate of U(VI) decreases with the increase of As(III) concentration, whereas the photooxidation rate of As(III) to As(V) increases with the increase of As(III) concentration. Especially, XPS analysis in time-scale firstly confirms the photoreduction of U(VI) to U(IV) and photooxidation of As(III) to As(V) in the photocatalytic process. In addition, it was demonstrated that ·O$_2^-$, ·OH and h^+ were main active species in the As(III) oxidation, and photogenerated electrons were used for the reduction of U(VI) to U(IV). A suitable mechanism was proposed to well explain the enhanced photocatalytic activity of the g-C$_3$N$_4$/TiO$_2$ and the competitive relationship between photoreduction of U(VI) and
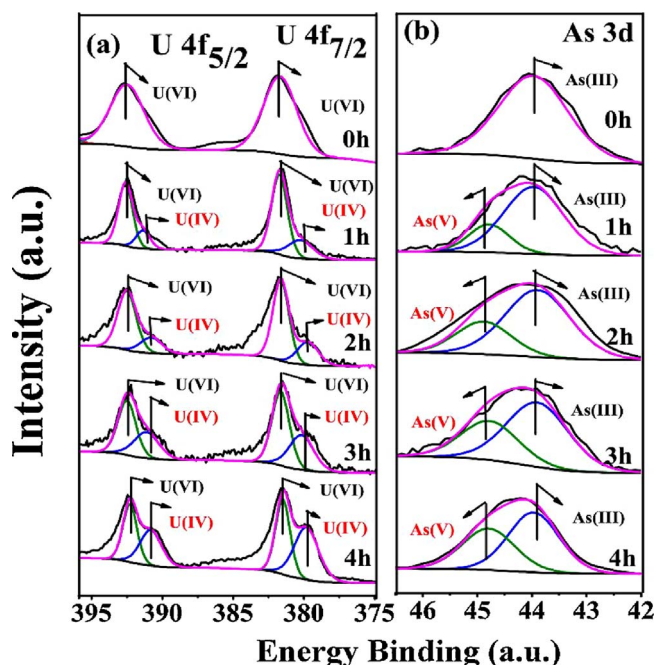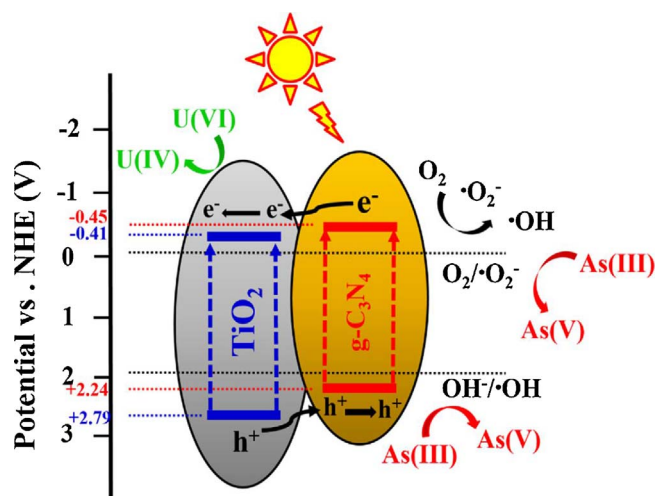
Scheme 1. Proposed mechanism of the simultaneously photoreduction of uranium(VI) and photooxidation of arsenic(III) in aqueous solution by the heterostructured g-C₃N₄/TiO₂ catalyst.

photooxidation of As(III). This work not only provides a photocatalytic system to achieve the simultaneous U(VI) photoreduction and As(III) photooxidation by one catalyst but also illuminates the relationship of photooxidation of As(III) and photoreduction of U(VI) for the first time.

Acknowledgements

Appendix A. Supplementary data

Supplementary material related to this article can be found, in the online version, at doi:https://doi.org/10.1016/j.apcatb.2018.01.062.

References

[1] H. Geckeis, J. Lutzenkirchen, R. Polly, T. Rabung, M. Schmidt, Chem. Rev. 113 (2013) 1016–1062.
[2] J.O. Nriagu, J.M. Pacyna, Nature 333 (1988) 134–139.
[3] S.J. Morrison, R.R. Spangler, Environ. Sci. Technol. 26 (1992) 1922–1931.
[4] M.J. Manos, M.G. Kanatzidis, J. Am. Chem. Soc. 134 (2012) 16441–16446.
[5] P.A. Bryant, J. Radiol. Prot. 34 (2014) N1–N6.
[6] A.C. Sather, O.B. Berryman, J. Rebek, J. Am. Chem. Soc. 132 (2010) 13572–13574.
[7] K.L. Cooper, E.J. Dashner, R. Tsosie, Y.M. Cho, J. Lewis, L.G. Hudson, Toxicol. Appl. Pharmacol. 291 (2016) 13–20.
[8] G. Mathews, N. Nagaiah, M.B.K. Kumar, M.R. Ambika, J. Radiol. Prot. 35 (2015) 447–455.
[9] I.K. Levy, M. Mizrahi, G. Ruano, G. Zampieri, F.G. Requejo, M.I. Litter, Environ. Sci. Technol. 46 (2012) 2299–2308.
[10] J. Ryu, D. Monllor-Satoca, D.H. Kim, J. Yeo, W. Choi, Environ. Sci. Technol. 47 (2013) 9381–9387.
[11] J. Bundschuh, M. Litter, V.S.T. Ciminelli, M.E. Morgada, L. Cornejo, S.G. Hoyos, J. Hoinkis, M.T. Alarcon-Herrera, M.A. Armienta, P. Bhattacharya, Water Res. 44 (2010) 5828–5845.
[12] J.M. Meichtry, I.K. Levy, H.H. Mohamed, R. Dillert, D.W. Bahnemann, M.I. Litter, ChemPhysChem 17 (2016) 885–892.
[13] J. Kim, J. Kim, Environ. Sci. Technol. 48 (2014) 13384–13391.
[14] W.L. Li, L.D. Troyer, S.S. Lee, J.W. Wu, C. Kim, B.J. Lafferty, J.G. Catalano, J.D. Fortner, ACS Appl. Mater. Interfaces 9 (2017) 13163–13172.
[15] V.S. Mehta, F. Maillot, Z.M. Wang, J.G. Catalano, D.E. Giammar, Water Res. 69 (2015) 307–317.
[16] H.B. Liu, M.X. Li, T.H. Chen, C.L. Chen, N.S. Alharb, T. Hayat, D. Chen, Q. Zhang, Y.B. Sun, Environ. Sci. Technol. 51 (2017) 9227–9234.
[17] M. Zegke, G.S. Nichol, P.L. Arnold, J.B. Love, Chem. Commun. 51 (2015) 5876–5879.
[18] M.H. Sun, S.Q. Liu, K.J. Du, C.M. Nie, Y.W. Lin, Spectrochim. Acta A Mol. Biomol. Spectrosc. 118 (2014) 130–137.
[19] H. Liu, K.C. Zuo, C.D. Vecitis, Environ. Sci. Technol. 48 (2014) 13871–13879.
[20] S. Vadahanambi, S.H. Lee, W.J. Kim, I.K. Oh, Environ. Sci. Technol. 47 (2013) 10510–10517.
[21] Z.H. Wang, R.T. Bush, L.A. Sullivan, C.C. Chen, J.S. Liu, Environ. Sci. Technol. 48 (2014) 3978–3985.
[22] D.H. Dang, B. Novotnik, W. Wang, R.B. Georg, R.D. Evans, Environ. Sci. Technol. 50 (2016) 12695–12704.
[23] S. Tresintsi, K. Simeonidis, S. Estrade, C. Martinez-Boubeta, G. Vourlias, F. Pinakidou, M. Katsikini, E.C. Paloura, G. Stavropoulos, M. Mitrakas, Environ. Sci. Technol. 47 (2013) 9699–9705.
[24] W. Liu, J.R. Ni, X.C. Yin, Water Res. 53 (2014) 12–25.
[25] Y. Choi, M.S. Koo, A.D. Bokare, D.H. Kim, D.W. Bahnemann, W. Choi, Environ. Sci. Technol. 51 (2017) 3973–3981.
[26] C.H. Lu, R.Y. Chen, X. Wu, M.F. Fan, Y.H. Liu, Z.G. Le, S.J. Jiang, S.Q. Song, Appl. Surf. Sci. 360 (2016) 1016–1022.
[27] L. Ke, P.F. Li, X. Wu, S.J. Jiang, M.B. Luo, Y.H. Liu, Z.G. Le, C.Z. Sun, S.Q. Song, Appl. Catal. B Environ. 205 (2017) 319–326.
[28] Z.J. Li, Z.W. Huang, W.L. Guo, L. Wang, L.R. Zheng, Z.F. Cha, W.Q. Shi, Environ. Sci. Technol. 51 (2017) 5666–5674.
[29] Y.X. Wang, J.M. Duan, W. Li, S. Beecham, D. Mulcahy, J. Hazard. Mater. 303 (2016) 162–170.
[30] J. Xu, J.J. Li, F. Wu, Y. Zhang, Environ. Sci. Technol. 48 (2014) 272–278.
[31] Z.Z. Pan, W.L. Li, J.D. Fortner, D.E. Giammar, Environ. Sci. Technol. 51 (2017) 9219–9226.
[32] S. Tripathi, R. Bose, A. Roy, S. Nair, N. Ravishankar, ACS Appl. Mater. Interfaces 7 (2015) 26430–26436.
[33] V.N. Salomone, J.M. Meichtry, M.I. Litter, Chem. Eng. J. 270 (2015) 28–35.
[34] J.P. Zou, D.D. Wu, S.K. Bao, J.M. Luo, X.B. Luo, S.L. Lei, H.L. Liu, H.M. Du, S.L. Luo, C.T. Au, S.L. Suib, ACS Appl. Mater. Interfaces 7 (2015) 28429–28437.
[35] X.L. Zhang, M.F. Wu, H. Dong, H.C. Li, B.C. Pan, Environ. Sci. Technol. 51 (2017) 6326–6334.
[36] V. Lenoble, V. Deluchat, B. Serpaud, J.C. Bollinger, Talanta 61 (2003) 267–276.
[37] Z. Luo, A.S. Poyraz, C.-H. Kuo, R. Miao, Y. Meng, S.-Y. Chen, T. Jiang, C. Wenos, S.L. Suib, Chem. Mater. 27 (2015) 6–17.
[38] J.S. Chen, Y.L. Tan, C.M. Li, Y.L. Cheah, D. Luan, S. Madhavi, F.Y.C. Boey, L.A. Archer, X.W. Lou, J. Am. Chem. Soc. 132 (2010) 6124–6130.
[39] J.-P. Zou, L.-C. Wang, J. Luo, Y.-C. Nie, Q.-J. Xing, X.-B. Luo, H.-M. Du, S.-L. Luo, S.L. Suib, Appl. Catal. B Environ. 193 (2016) 103–109.
[40] X. Chen, J. Wei, R. Hou, Y. Liang, Z. Xie, Y. Zhu, X. Zhang, H. Wang, Appl. Catal. B Environ. 188 (2016) 342–350.
[41] H.W. Huang, X. Han, X.W. Li, S.C. Wang, P.K. Chu, Y.H. Zhang, ACS Appl. Mater. Interfaces 7 (2015) 482–492.
[42] Z. Dai, F. Qin, H.P. Zhao, J. Ding, Y.L. Liu, R. Chen, ACS Catal. 6 (2016) 3180–3192.
[43] Z.Q. Li, H.L. Wang, L.Y. Zi, J.J. Zhang, Y.S. Zhang, Ceram. Int. 41 (2015) 10634–10643.
[44] L.L. Cheng, S.F. Zhang, Y.J. Wang, G.J. Ding, Z. Jiao, Mater. Res. Bull. 73 (2016) 77–83.
[45] H.J. Sun, A.D. Zhao, N. Gao, K. Li, J.S. Ren, X.G. Qu, Angew. Chem. Int. Ed. 54 (2015) 7176–7180.
[46] X. Zhang, M. Wu, H. Dong, H. Li, B.-C. Pan, Environ. Sci. Technol. 51 (2017) 6326–6334.
[47] X. Song, Y. Hu, M. Zheng, C. Wei, Appl. Catal. B Environ. 182 (2016) 587–597.
[48] J.-P. Zou, D.-D. Wu, J. Luo, Q.-J. Xing, X.-B. Luo, W.-H. Dong, S.-L. Luo, H.-M. Du, S.L. Suib, ACS Catal. 6 (2016) 6861–6867.
[49] A. Hierro, J.E. Martin, M. Olias, F. Vaca, J.P. Bolivar, Water Res. 47 (2013) 6269–6279.
[50] M.Y. Xu, X.L. Han, D.B. Hua, J. Mater. Chem. A 5 (2017) 12278–12284.
[51] F. Yuan, C.F. Wu, Y.W. Cai, L.J. Zhang, J.Q. Wang, L.H. Chen, X.K. Wang, S.T. Yang, S.A. Wang, Chem. Eng. J. 322 (2017) 353–365.
[52] M. Yoon, Y. Oh, S. Hong, J.S. Lee, R. Boppella, S.H. Kim, F.M. Mota, S.O. Kim, D.H. Kim, Appl. Catal. B Environ. 206 (2017) 263–270.